Journal of Cleaner Production 215 (2019) 1341–1350

Contents lists available at ScienceDirect

Journal of Cleaner Production

journal homepage: www.elsevier.com/locate/jclepro

Sonocatalytic degradation of Acid Red 1 by sonochemically synthesized zinc sulfide-titanium dioxide nanotubes: Optimization, kinetics and thermodynamics studies

Ali Mehrizad [a, *], Mohammad A. Behnajady [a], Parvin Gharbani [b], Shervin Sabbagh [a]

[a] Department of Chemistry, Tabriz Branch, Islamic Azad University, Tabriz, Iran
[b] Department of Chemistry, Ahar Branch, Islamic Azad University, Ahar, Iran

ARTICLE INFO

Article history:
Received 22 October 2018
Received in revised form
7 January 2019
Accepted 15 January 2019
Available online 18 January 2019

Keywords:
Sonocatalysis
ZnS
TiO_2 nanotubes
Acid red 1
RSM
Kinetics
Thermodynamics

ABSTRACT

The present study reports sonocatalytic activity of zinc sulfide-titanium dioxide nanotubes (ZnS-TNTs) in degradation of Acid Red 1 (AR1). Co-precipitation, hydrothermal and sonochemical methods were used to synthesize ZnS, TNTs and ZnS-TNTs, respectively. The physicochemical characteristics of the synthesized powders were determined by XRD, FE-SEM, TEM, SAED, EDX, UV–Vis, BET and BJH techniques. The effect of the operational parameters on the sonocatalytic process was evaluated and optimized using the response surface methodology. Under optimal conditions (initial AR1 concentration = 15 mg L^{-1}, ZnS-TNTs amount = 1 g L^{-1}, pH = 6, ultrasonic power = 75 W and time = 20 min), more than 75% of the dye molecules were degraded. The Langmuir-Hinshelwood's kinetics model was well obeyed by the involved process (k_{ap} = 0.0631 min^{-1}). The thermodynamics of the process was studied based on the transition state theory and it was found that the sonocatalytic process was endothermic and nonspontaneous. Ultimately, the main products of AR1 degradation were identified by the GC-MS technique.

1. Introduction

The most important type of commercial dyes refers to azo dyes, comprising over 50% of the global production of dyes. The characteristic feature of these dyes is the presence of one or more azo bonds (-N=N-) in their chemical structure. Azo dyes are introduced into the industrial wastewaters at different stages of dyeing and textiles, and discharging them into aquatic environments leads to serious problems to flora and fauna (Ledakowicz et al., 2017; Aljerf, 2018). Various physicochemical and biological methods have been proposed to eliminate such pollutants, which are often not interesting due to transfer of pollutants from one phase to another or lack of biological degradation (Miner et al., 2017; Di Nica et al., 2017; Saratale et al., 2011; Sen et al., 2016). Among the developed treatment methods, advanced oxidation processes (AOPs) have been proved to be more effective as they can degrade a wide range of pollutants (Silva et al., 2018). Sonocatalysis is one of the AOPs relying on the simultaneous presence of an appropriate semiconductor catalyst and ultrasound (US) irradiation (Adewuyi, 2001). The degradation mechanism of sonocatalytic processes is mainly based on the hot-spot theory and the sonoluminescence phenomenon. According to the hot-spot theory, most physical and chemical effects of US are related to a process called cavitation, which is defined as the formation, growth and collapse of microbubbles within an aqueous solution. Owing to the collapse of the bubbles, a shock wave is produced causing a localized temperature and pressure. Such extraordinary conditions can lead to pyrolysis of water molecules and formation of hydrogen and hydroxyl radicals (°H and °OH), as well as the thermal excitation of electron from the valence band (VB) to the conduction band (CB) of the semiconductor catalyst. In addition, the collapse of the bubbles generates some picosecond flashlights known as sonoluminescence irradiation. This irradiation, in turn, can create electron-hole (e^--h^+) pairs with light stimulation of the semiconductor (Eren and Ince, 2010; Leong et al., 2011; Qiu et al., 2018). In this regard, titanium dioxide (TiO_2) is one of the most commonly used semiconductors in the field of sonocatalysis. The catalytic activity of TiO_2 is mainly influenced by its crystalline structure (anatase, rutile and brookite) and morphology (nanoparticle, nanowire, nanotube etc.) (Wang et al., 2005, 2007, 2010; Song et al., 2012; Khataee et al.,

* Corresponding author.
E-mail address: mehrizad@iaut.ac.ir (A. Mehrizad).

https://doi.org/10.1016/j.jclepro.2019.01.172
0959-6526/

2016). It has been reported that the sonocatalytic performance of TiO_2 nanotubes (TNTs) is far more than that of nanoparticles, which can be attributed to its distinct properties such as tubular structure, high surface area and pore volume (Pang et al., 2010, 2011; Pang and Abdullah, 2012). However, there are still some problems restricting the sonocatalytic application of TNTs. Diverse strategies have been proposed to enhance the sonocatalytic efficiency of TNTs like incorporation of titania nanotubes with Fe^{3+}, γ-Fe_2O_3, carbon and nitrogen (Pang and Abdullah, 2013a, 2013b; Pang et al., 2016; Alwash et al., 2013), but it has not yet been addressed for the ZnS-TNTs sonocatalytic activity.

In the present study, co-precipitation, hydrothermal and sonochemical methods were used to synthesize the ZnS, TNTs and ZnS-TNTs samples, respectively. The sonocatalytic activity of the samples was scanned by degradation of Acid Red 1 (AR1) as a model azo dye. Modeling and optimizing the sonocatalytic degradation of AR1 by ZnS-TNTs were performed using the response surface methodology (RSM). The optimized process was also studied from kinetics and thermodynamics perspectives.

2. Experimental

2.1. Materials

Titanium dioxide nanopowder (TiO_2-P25) was purchased from Degussa (Germany). Sodium hydroxide (NaOH, 97%), hydrochloric acid (HCl, 37%), zinc acetate dihydrate ($Zn(CH_3COO)_2.2H_2O$) and sodium sulfide (Na_2S) were obtained from Merck (India). Azo Acid Red 1 dye ($C_{18}H_{13}N_3Na_2O_8S_2$, $\lambda_{max} = 532$ nm, Fig. S1) was procured from Sigma-Aldrich (USA).

2.2. Synthesis of ZnS

ZnS particles were synthesized through a co-precipitation method. At first, 4.39 g of $Zn(CH_3COO)_2.2H_2O$ was dissolved in 100 mL deionized water, the prepared 0.2 M solution was poured into a flask and magnetically stirred for 15 min at 200 rpm. Then, 100 mL Na_2S (0.2 M) was gradually added into the flask under the presence of Ar gas, and the reaction was allowed to proceed under vigorous stirring (600 rpm) for 90 min. The white precipitates were collected by suction filtration, washed thoroughly with acetone and deionized water, and dried at room temperature.

2.3. Synthesis of TNTs

TNTs were prepared by a hydrothermal method. First, 4.5 g of TiO_2-P25 was added into 270 mL NaOH (10 M) under sonication and the obtained mixture was transferred into a 300 mL autoclave reactor. Next, the reactor was placed in an oil bath at 120 °C for 30 h. The resulting mixture was filtered and washed with deionized water for several times. The precipitates were stirred with 100 mL of HCl (1 M) for 4 h to trim down high basic nature and then rinsed with deionized water for several times as the pH of the rinsing solution reached 6.5. Finally, the obtained product was allowed to drying in an oven at 110 °C and calcined at 400 °C for 3 h in a furnace.

2.4. Synthesis of ZnS-TNTs composite

The fabrication of ZnS-TNTs composite was carried out using an ultrasonic homogenizer (SONOPULS, HD 3200). At first, 100 mL $Zn(CH_3COO)_2.2H_2O$ (0.5 M) was poured in a 3-neck round-bottomed flask underwent US waves. Then, TNTs (3g) were dispersed into the zinc acetate solution under sonication. Afterward, 100 mL Na_2S (0.5 M) was gradually added into the flask under the presence of Ar gas and the reaction was allowed to proceed under sonication for 45 min. The resulting precipitates were collected by suction filtration, washed thoroughly with acetone and deionized water, and dried at room temperature.

2.5. Characterization techniques

The crystallite structures of the synthesized samples (ZnS, TNTs and ZnS-TNTs) were characterized by an X-ray diffraction (XRD, X'Pert Pro, Panalytical). Field emission-scanning electron microscope (FE-SEM, SIGMA, Zeiss), transmission electron microscope (TEM, Zeiss-EM10C-100 kV, FEI, Tecnai F 20) were used to descry the morphological properties of the specimens. UV–Vis spectra were studied using a UV-2550 Shimadzu spectrophotometer. Quantachrome Nova 2000e surface area and pore size analyzer was used to determine the specific surface area and pore size distribution of the samples by Brunauer-Emmett-Teller (BET) and Barrett-Joyner-Halenda (BJH) methods, respectively. The main products of AR1degradation were identified by a gas chromatograph (GC, Agilent 6890) coupled with a mass spectrometer (MS, Agilent 5973). To prepare the sample for GC-MS analysis, extraction of organics from the solution was carried out using diethyl ether. The collected organic solution was evaporated and the residue was dissolved in N,O-bis-(trimetylsilyl)acetamide. Thereafter, a GC with a 30 m to 0.25 mm HP-5MS capillary column coupled with a MS operating in EI mode at 70 eV was utilized for analysis by the temperature program of 50 °C for 4 min, 8 °C min^{-1} up to 300 °C and hold time of 4 min.

2.6. Sonocatalytic experiments

Experiments were conducted in a round-bottomed flask equipped with a water bath under US waves of a probe sonicator (SONOPULS, HD3200). In each experiment, a predefined amount of catalyst was mixed with 100 mL of AR1 solution at a given initial concentration and pH. To assure about adsorption-desorption of dye on the catalyst samples, the obtained suspension was initially stirred on a magnetic stirrer (IKA, RH Basic2) in the dark for 30 min. Then, the suspension was ultrasonicated and sampled at the time intervals listed in Table 1. Absorbance and concentration of the centrifuged samples were determined using UV–Vis spectrophotometer (UV mini-1240 Shimadzu) and calibration curve, respectively. The removal or degradation efficiency of dye was calculated from Eq. (1):

$$Efficiency\ (\%) = \left(1 - \frac{[AR1]}{[AR1]_0}\right) \times 100 \quad (1)$$

where $[AR1]_0$ and $[AR1]$ are the dye concentration (mg L^{-1}) at initial and certain reaction time, respectively.

2.7. Design of experiments

To save time and expenses, the experiments were designed in the framework of central composite design (CCD) based on RSM with the help of the Design-Expert® 11 software. According to a series of preliminary experiments, the operational parameters affecting the process were identified and their ranges were determined. Table 1 presents the domain of the parameters along with fifty designed tests (50 runs).

3. Results and discussion

3.1. Characterization of the synthesized powders

The XRD patterns of ZnS, TNTs and ZnS-TNTs are portrayed in

Table 1
Domain of the parameters and design layout along with experimental and theoretical results.

Operational parameters	Levels (coded and uncoded)				
	-α (−2)	−1	0	+1	+α (+2)
A: $[AR1]_0$ (mg L^{-1})	10	15	20	25	30
B: $[Catalyst]_0$ (g L^{-1})	0.25	0.5	0.75	1	1.25
C: pH	2	4	6	8	10
D: US power (W)	30	45	60	75	90
E: Time (min)	5	10	15	20	25

Run	Parameters in terms of coded levels					Efficiency (%)	
	A: [AR1] 0	B: [Catalyst] 0	C: pH	D: US power	E: Time	Experimental	Theoretical
1	1	1	−1	1	−1	54.16	56.82
2	0	0	0	−2	0	49.17	51.24
3	1	−1	1	−1	−1	35.02	33.81
4	0	0	0	0	0	49.83	51.22
5	−1	1	−1	1	−1	65.62	65.93
6	−1	−1	−1	1	−1	68.31	68.33
7	1	1	−1	1	1	70.18	69.34
8	−1	1	1	−1	1	69.80	68.04
9	−1	1	−1	−1	1	58.98	62.44
10	0	0	0	0	0	48.83	51.22
11	−1	1	1	−1	−1	53.78	56.90
12	−1	1	1	1	−1	61.44	63.53
13	−1	−1	−1	1	1	75.33	74.84
14	2	0	0	0	0	39.37	38.64
15	−1	−1	−1	−1	1	61.67	59.34
16	0	0	0	0	2	76.85	75.02
17	1	−1	−1	1	1	67.87	65.74
18	−1	−1	1	−1	1	57.50	57.81
19	1	−1	−1	−1	−1	39.20	40.59
20	0	−2	0	0	0	48.52	49.39
21	−1	−1	−1	−1	−1	50.65	53.44
22	1	−1	−1	−1	1	50.22	49.35
23	1	1	1	−1	1	58.34	57.81
24	1	1	−1	−1	1	52.52	55.33
25	0	0	0	0	−2	54.81	54.48
26	1	−1	−1	1	−1	53.86	56.34
27	0	0	−2	0	0	55.00	53.27
28	0	0	0	2	0	78.49	74.26
29	−1	1	−1	1	1	71.63	75.57
30	1	−1	1	1	1	49.70	55.21
31	1	1	1	−1	−1	42.33	43.79
32	−1	−1	1	1	1	65.15	67.44
33	0	0	2	0	0	46.65	46.22
34	−1	1	1	1	1	77.46	75.30
35	−1	−1	1	1	−1	59.14	58.80
36	1	1	1	1	−1	49.98	51.30
37	1	−1	1	1	−1	47.68	43.69
38	0	0	0	0	0	53.83	51.22
39	−1	−1	1	−1	−1	51.48	49.79
40	1	−1	1	−1	1	46.04	44.70
41	0	0	0	0	0	50.83	51.22
42	0	2	0	0	0	63.13	60.10
43	0	0	0	0	0	47.83	51.22
44	−1	1	−1	−1	−1	57.96	53.42
45	1	1	1	1	1	66.00	65.94
46	0	0	0	0	0	54.83	51.22
47	1	1	−1	−1	−1	46.50	43.44
48	0	0	0	0	0	49.83	51.22
49	0	0	0	0	0	51.83	51.22
50	−2	0	0	0	0	62.28	60.85

Fig. 1. For ZnS, all the peaks are in accordance with the cubic crystalline structure of ZnS and the plans (111), (220) and (311) are clearly indexed (JCPDS Card No. 65–0309) (Fang et al., 2011). The diffraction pattern of TNTs shows low crystallinity with some of the peaks from the TiO_2 anatase phase (JCPDS Card No. 21–1272) (Eskandarloo et al., 2016). It is well seen that the XRD pattern of the ZnS-TNTs composite includes the characteristic peaks of their counter parts (ZnS and TNTs), which reveals that ZnS nanoparticles

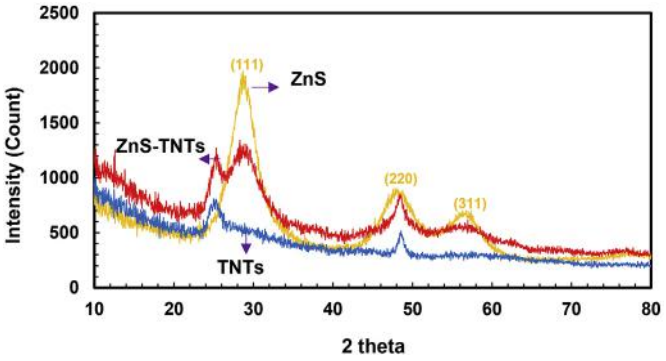

Fig. 1. XRD patterns of ZnS, TNTs and ZnS-TNTs powders.

are successfully embedded in TNTs matrix.

The intact morphology of the synthesized samples was analyzed by FE-SEM and TEM. Fig. 2 (a) shows the formation of the ZnS spherical nanoparticles, and Fig. 2 (b) confirms the tubular structure of the pure TNTs. The closer investigation of ZnS-TNTs by a relatively high magnification TEM (Fig. 2c) demonstrates that the TNTs are unevenly decorated with ZnS nanoparticles along the length. Additionally, from the selected area electron diffraction pattern (SAED, inset of Fig. 2c), many grown ZnS particles are clearly seen on the surface of TNTs. The EDX spectrum (Fig. 2d) also indicates the presence of elemental Zn and S signals, confirming the existence of ZnS on TNTs consistent with the XRD results.

The UV–Vis absorption spectra (Fig. 3) and Eq. (2) were used to estimate the band gap energy of synthesized samples.

$$E_{bg} = \frac{1240}{\lambda} \quad (2)$$

where E_{bg} and λ are the band gap energy (eV) and wavelength of maximum absorbance (nm), respectively (Ran et al., 2016). The calculated values of E_{bg} for ZnS, TNTs and ZnS-TNTs are 3.35, 3.22 and 3.02 eV, respectively.

Textural properties of the samples such as the specific surface area, mean pore diameter and pore volume were determined using BET and BJH methods. Fig. 4 represents N_2 adsorption/desorption isotherms with the pore size distribution curves, and Table 2 summarizes the results. Type of isotherms (IV) and hysteresis loops (H3) reveal the mesoporous nature of the samples (Thommes et al., 2015). In addition, it is obvious that the surface area of ZnS-TNTs slightly decreased compared to TNTs, which can be attributed to the surface covering of TNTs by ZnS.

3.2. Sonolysis, adsorption and sonocatalysis

The effect of sonolysis (US), adsorption (ZnS, TNTs and ZnS-TNTs) and sonocatalysis (ZnS + US, TNTs + US and ZnS-TNTs + US) on the removal of AR1 from aqueous solution was investigated, and Fig. 5 illustrates the results. As can be seen, ZnS-TNTs composite in the presence of US waves plays the main role in the removal of AR1 (54.38%). Removal of dye by sonolysis (19.78%) is mostly related to the attack of °H and °OH radicals caused by the cavitation pyrolysis of H_2O molecules. The adsorption sequence of ZnS-TNTs (40.97) » TNTs (36.21) »» ZnS (5.42) is also mainly due to high surface area and large pore volume of TNTs structure. However, the high removal efficiency of dye with the ZnS-TNTs sonocatalytic process can be ascribed to the i) high adsorption due to the large surface area of the TNTs; ii) enhancement of the bubble nucleation for the cavitation process due to presence of ZnS particles and TNTs and iii) photo-thermal catalytic processes of ZnS and

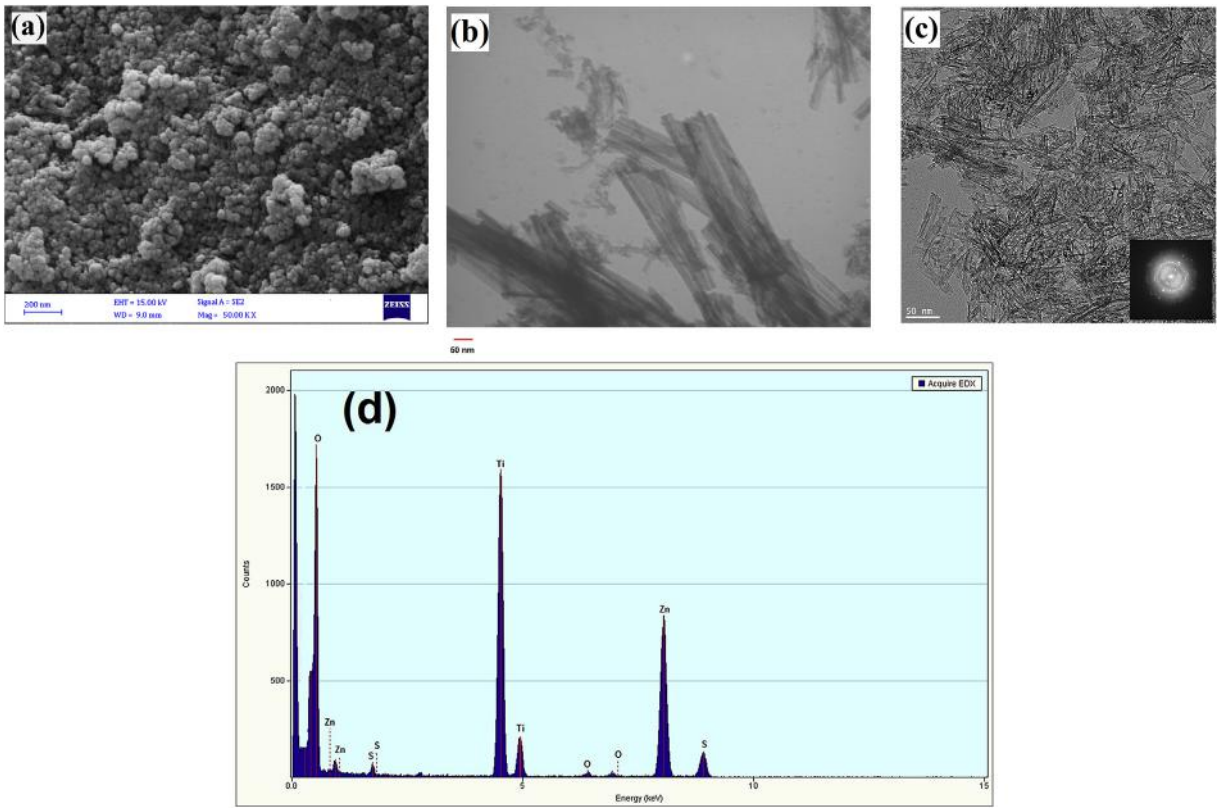

Fig. 2. (a) FE-SEM image of ZnS, (b) TEM image of TNTs, (c) TEM image of ZnS-TNTs and (d) EDX spectrum of ZnS-TNTs.

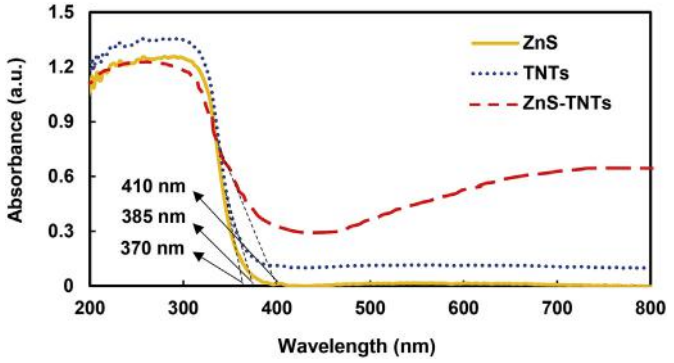

Fig. 3. UV–Vis absorption spectra of ZnS, TNTs and ZnS-TNTs.

TNTs due to the considerable localized temperature and sonoluminescence phenomenon. These justifications are inspired by the literature review (Adewuyi, 2001; Leong et al., 2011; Qiu et al., 2018; Franc and Michel, 2006) and Section 3.6 explains it in detail.

In continuation of our investigations, sonocatalytic degradation of AR1 by ZnS-TNTs was explored by RSM and followed by kinetics and thermodynamics studies.

3.3. Modeling and optimization of the sonocatalytic process by RSM

As aforementioned in Section 2.7, the experiments were designed by RSM-CCD and 50 tests were performed based on the software offer (Table 1). After registering the experimentally results in the DX11 software, a quadratic polynomial model was proposed to fit the response (theoretical efficiency) versus the operational parameters (see Table 3) (Bezerra et al., 2008).

Analysis of variance (ANOVA) was used to assess reliability of the proposed model and the results are presented in Table 4.

According to the ANOVA results, the model F-value of 26.92 and p-value of <0.0001 represent the model's veracity. The lack of fit F-value of 1.76 implies the lack of fit is not significant relative to the pure error. Also, the correlation coefficient (R^2) of 0.9489 is in fair agreement with the adjusted R^2 value of 0.9136, i.e. there is a significant relevance between the experimental and theoretical values of efficiency, which is well illustrated in Fig. S2.

Pursuant to the statistical principles, p-values less than 0.0500 indicate model terms are significant and conversely, values greater than 0.1000 indicate the model terms are not significant. In this case A, B, D, E, D^2 and E^2 are significant model terms.

For a more accurate assessment of the effect of each operational parameter on the sonocatalytic process, Pareto analysis was employed according to Eq. (3):

$$P_i = \left(\frac{\beta_i^2}{\sum \beta_i^2}\right) \times 100 \; i \neq 0 \tag{3}$$

where β_i and P_i are the coefficient (see Table 3) and percentage effect of each term, respectively (Aghaeinejad-Meybodi et al., 2015). Fig. 6 shows that US power (D), initial dye concentration (A), irradiation time (E) and catalyst amount (B) are remarkable model terms, which is supported by p-values of terms.

Based on the variance and Pareto analyses, response surface diagrams (Fig. 7) were used to visualize the effects of the four main parameters (A, B, D and E) on the efficiency of AR1 sonocatalytic degradation.

According to Fig. 7, the degradation efficiency of AR1 increases with the increase of catalyst amount, US power and time, and reduces with the increment of the dye initial concentration. As

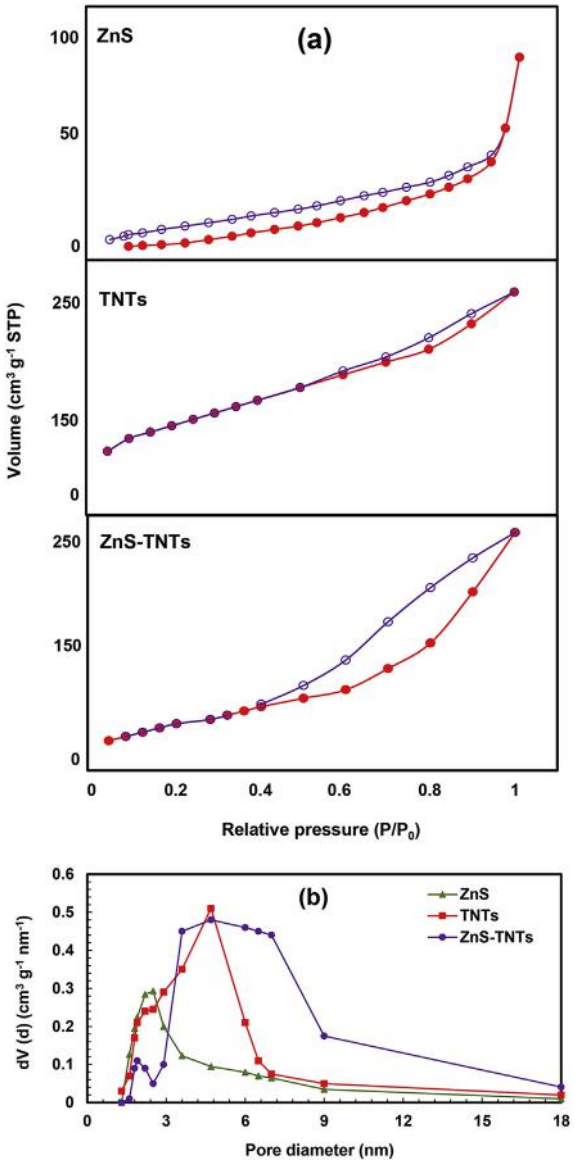

Fig. 4. (a) N_2 adsorption/desorption isotherms and (b) BJH pore size distribution curves.

previously explained, the presence of a semiconductor catalyst in sonocatalytic processes is associated with two important roles. First, semiconductor particles enhance bubble nucleation and, therefore, cavitation and generation of °H and °OH radicals via water pyrolysis. Second, the production of picosecond flashlights by the sonoluminescence phenomenon stimulates the semiconductor and causes generation of e^--h^+ pairs (Adewuyi, 2001; Leong et al., 2011; Qiu et al., 2018; Franc and Michel, 2006). The generated holes were combined with water molecules and hydroxide anions (OH^-) to form hydroxyl radicals (°OH). Meantime, the released electrons were reload with dissolved oxygen molecules to produce superoxide anions ($^{\circ}O_2^-$). Therefore, increasing the amount of catalyst can lead to production of more active species and, consequently, improvement of the degradation process. Moreover, high surface area of TNTs promotes dye adsorption and contributes to progress of the degradation process.

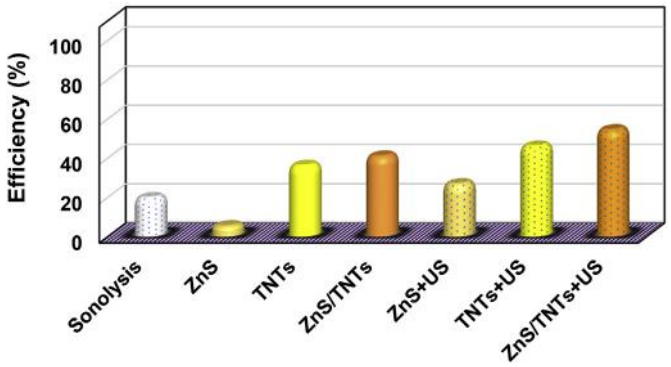

Fig. 5. Comparison of AR1 removal by sonolysis, adsorption and sonocatalysis. ($[AR1]_0 = 20\ mg\ L^{-1}$; [Adsorbent or Catalyst]$_0 = 0.75\ g\ L^{-1}$; pH = 6; US power = 60 W; Time = 30 min).

Generally, the power and duration of ultrasonication play key roles in sonocatalytic processes. Loading higher power at longer times leads to increasing the energy of the system; as a result, it promotes cavitation. Concretely speaking, high power of US waves enlarge the produced bubbles and increase the intensity of the shock wave generated upon collapse of the bubbles (Richards and Loomis, 1927). The result of such events is an increase in the number of active species derived from the pyrolysis of water and sonoluminescence-based stimulation of the catalyst. In addition, increasing the US power facilitates transfer of dye molecules from the liquid phase to the surface of the catalyst, which improves dye degradation.

Reducing the degradation efficiency by increasing the initial dye concentration can be attributed to several reasons. First, increasing the number of dye molecules results in occupation of a greater number of active catalyst sites restricting absorption of the heat and energy released upon collapse of the acoustic bubbles. The second reason is associated with the fact that the presence of a higher number of dye molecules increases solution turbidity; therefore, scattering of the flashlights produced by sonoluminescence. Furthermore, with increasing dye concentration under operating conditions, the constant number of active species cannot respond to the amplified AR1 molecules, and thus the efficiency is reduced (Grčić et al., 2013; Darvishi Cheshmeh Soltani et al., 2016).

Since the objective of experimental design was to maximize dye degradation, the sonocatalytic process was optimized by DX11

Table 2
BET and BJH parameters of ZnS, TNTs and ZnS-TNTs.

Sample	S_{BET} ($m^2\ g^{-1}$)[a]	r_p (nm)[b]	V_{pore} ($cm^3\ g^{-1}$)[c]	Type of isotherm and hysteresis loop[d]
ZnS	43.29	2.2	0.28	IV, H3
TNTs	248.54	4.7	0.51	IV, H3
ZnS-TNTs	208.03	3.3	0.48	IV, H3

[a] Specific surface area determined by the BET method.
[b] Average pore size obtained by the BJH method.
[c] Total pore volume determined from the volume of N_2 adsorbed at $P/P_0 = 0.990$.
[d] Type of isotherm and hysteresis loop as specified in the IUPAC manual (Thommes et al., 2015).

Table 3
Quadratic polynomial model.

Quadratic polynomial model	
General form	$y = \beta_0 + \sum_{i=1}^{k}\beta_i x_i + \sum_{i=1}^{k}\sum_{j=1}^{k}\beta_{ij}x_i x_j + \sum_{i=1}^{k}\beta_{ii}x_i^2$ [a]
This research (Coded equation)	*Theoretical efficiency* (%) $= 51.23 - 5.55A + 2.68B - 1.76C + 5.75D + 5.13E + 0.7188AB - 0.7813AC + 0.2188AD + 0.7188AE + 1.78BC - 0.5938BD + 0.7812BE - 1.47CD + 0.5312CE + 0.1562DE - 0.3688A^2 + 0.8812B^2 - 0.3688C^2 + 2.88D^2 + 3.38E^2$

[a] y: Theoretical response; k: Number of operational parameters; β_0: Constant; β_i, β_{ij} and β_{ii}: Coefficients for linear, reciprocal, and quadratic effects, respectively; x_i and x_j: operational parameters (Bezerra et al., 2008).

Table 4
ANOVA results for the proposed model.

Source	Sum of Squares	Degree of freedom	Mean Square	F-value	p-value
Model	4953.34	20	247.66	26.92	<0.0001
A	1233.54	1	1233.54	134.08	<0.0001
B	286.70	1	286.70	31.16	<0.0001
C	124.29	1	124.29	13.51	0.1289
D	1324.22	1	1324.22	143.94	<0.0001
E	1054.21	1	1054.21	114.59	<0.0001
AB	16.53	1	16.53	1.796	0.1905
AC	19.53	1	19.53	2.12	0.1558
AD	1.531	1	1.531	0.16	0.6863
AE	16.53	1	16.53	1.79	0.1905
BC	101.53	1	101.53	11.03	0.2024
BD	11.28	1	11.28	1.22	0.2772
BE	19.53	1	19.53	2.12	0.1558
CD	69.03	1	69.03	7.50	01104
CE	9.03	1	9.031	0.98	0.3300
DE	0.78	1	0.78	0.08	0.7728
A^2	4.35	1	4.35	0.47	0.4971
B^2	24.85	1	24.85	2.70	0.1111
C^2	4.35	1	4.35	0.47	0.4971
D^2	265.65	1	265.65	28.87	<0.0001
E^2	365.84	1	365.84	39.76	<0.0001
Residual	266.79	29	9.02		
Lack of Fit	255.91	22	10.27	1.76	0.2267
Pure Error	40.88	7	5.84		
Cor Total	5220.13	49			

Quality of quadratic model	
R2	Adjusted R2
0.9489	0.9136

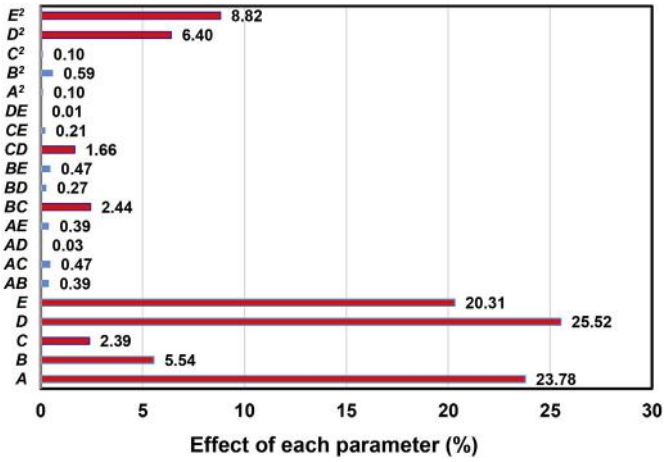

Fig. 6. Pareto graphic analysis.

software. Under optimal conditions (initial AR1 concentration of 15 mg L^{-1}, ZnS-TNTs amount of 1 g L^{-1}, pH 6, US power of 75 W and

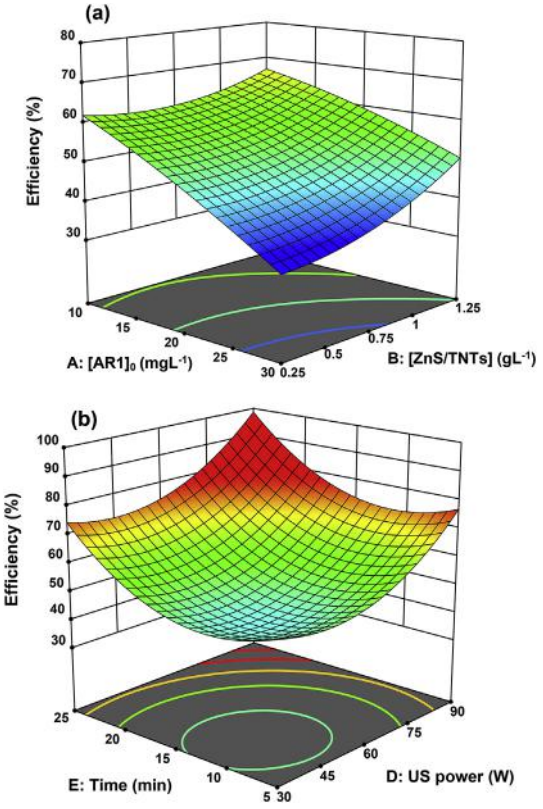

Fig. 7. Response surface diagrams of the sonocatalytic efficiency as a function of (a) concentrations of AR1 and ZnS-TNTs; (b) US power and irradiation time.

20 min of US irradiation exposure), the theoretical efficiency of dye degradation was 75.5%. Performing the experiments under optimal conditions revealed that approximately 73% of AR1 was degraded, confirming the accuracy and validity of the proposed model by RSM.

To assess the reusability of the ZnS-TNTs nanocomposite, cyclic tests were conducted under RSM-based optimized conditions. The used catalyst was regenerated by filtering, washing and drying, and then it was reused in experiments. As Fig. S3 (a) shows, there is a 25% decrease in the catalyst efficiency after five run, which XRD pattern of the used ZnS-TNTs (Fig. S3 b) indicates the outstanding chemical stability of nanocomposite. It suggests that the ZnS-TNTs nanocomposite could be used as a robust and durable catalyst in purification processes.

3.4. Kinetics of the sonocatalytic process

Inspired by literature review (Grčić et al., 2013; Khataee et al., 2017; Yetim and Tekin, 2017), the kinetics of the sonocatalytic degradation of AR1 by ZnS-TNTs was studied using the Langmuir-Hinshelwood's model:

$$-\frac{d[AR1]}{dt} = \frac{kK[AR1]}{1 + K[AR1]_0} \quad (4)$$

where k and K are respectively the constants of reaction rate (mg L^{-1} min^{-1}) and adsorption equilibrium (L mg^{-1}). In highly diluted solution of dye, the term of $K[AR1]_0$ becomes less than 1 ($K[AR1]_0 << 1 \rightarrow 1 + K[AR1]_0 \approx 1$) and under these circumstances:

$$-\frac{d[AR1]}{dt} = kK[AR1] \quad (5)$$

By considering the apparent rate constant ($k_{ap} \approx kK$), Eq. (5) can be written as a pseudo-first-order model:

$$-\frac{d[AR1]}{dt} = k_{ap}[AR1] \longrightarrow [AR1] = [AR1]_0 \exp(-k_{ap}t) \quad (6)$$

In order to infer the reaction kinetics, several experiments were performed under the RSM-based optimized conditions at different time intervals (0–20 min) and room temperature (298 K). It can be concluded from Fig. 8, the sonocatalytic degradation of AR1 by ZnS-TNTs follows the pseudo-first-order model ($k_{ap} = 0.063$ min^{-1}).

To evaluate the influence of temperature on the reaction rate, the experiments were carried out in the temperature range of 298–318 K. It was found from the exponential curves (Fig. S4), the extent of the reaction was somewhat accelerated by raising the temperature (0.063, 0.073 and 0.087 min^{-1} at 298, 308 and 318 K, respectively).

The Arrhenius equation was employed to calculate the activation energy of reaction (E_a) and the frequency factor (A):

$$k_{ap} = A \exp\left(-\frac{E_a}{RT}\right) \rightarrow \ln k_{ap} = -\frac{E_a}{R}\cdot\frac{1}{T} + \ln A \quad (7)$$

where R and T are the universal gas constant (8.314 J K^{-1} mol^{-1}) and absolute temperature (K), respectively (Atkins and De Paula, 2009). E_a and A were obtained from the slope and intercept of the $\ln k_{ap}$-$1/T$ plot (Fig. S5), which respectively gave the 12.68 kJ mol^{-1} and 10.47 min^{-1} values.

In continuation of kinetics studies, the effect of each parameter within the range listed in Table 1 was evaluated by considering the values of other parameters at the central point (level = 0). As Fig. 9 and S6 show, the sonocatalytic degradation rate of AR1 increases with increment of catalyst amount and US power, whereas it decreases with increasing initial dye concentration. In addition, the pH of solution had no significant effect on the dye degradation rate. These results are in good agreement with the three-dimensional graphs (Fig. 7).

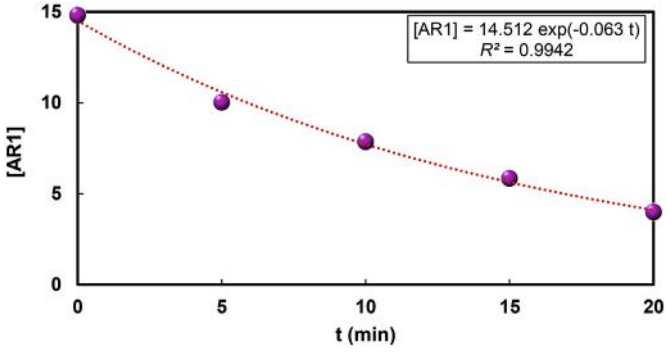

Fig. 8. Exponential plot of AR1 concentration versus time.

3.5. Thermodynamics of the sonocatalytic process

The thermodynamics of the sonocatalytic degradation of AR1 by ZnS-TNTs was studied using the Henry Eyring's transition state theory (TST) (Laidler and King, 1983).

Pursuant to the TST, the reaction rate of pre-equilibrium of $A + B \underset{k_{-1}}{\overset{k_1}{\rightleftharpoons}} AB^{\dagger} \longrightarrow P$ can be described as follows:

$$r = \frac{k_B T}{h}[AB^{\dagger}] \longrightarrow r = \frac{k_B T}{h}K^{\dagger}[A][B] \rightarrow k = \frac{k_B T}{h}K^{\dagger} \quad (8)$$

where r refers to the rate of reaction, and k_B, h, $K^{\dagger}$ and k are respectively the constants of Boltzmann (1.38×10^{-23} J K^{-1}), Plank (6.62×10^{-34} J s^{-1}), reaction equilibrium and rate.

The thermodynamics relationship between the equilibrium constant and Gibbs energy of activation ($\Delta G^{\dagger}$) is as follows:

$$\Delta G^{\dagger} = -RT \ln K^{\dagger} \quad \text{or} \quad K^{\dagger} = \exp\left(-\frac{\Delta G^{\dagger}}{RT}\right) \quad (9)$$

By substituting $K^{\dagger}$ from Eq. (9) into Eq. (8), the rate constant becomes:

$$k = \frac{k_B T}{h}\exp\left(-\frac{\Delta G^{\dagger}}{RT}\right) \quad (10)$$

Furthermore, $\Delta G^{\dagger}$ is given by $\Delta G^{\dagger} = \Delta H^{\dagger} - T\Delta S^{\dagger}$ and Eq. (10) can be written as:

$$k = \frac{k_B T}{h}\exp\left(-\frac{\Delta H^{\dagger}}{RT}\right)\exp\left(\frac{\Delta S^{\dagger}}{R}\right) \quad (11)$$

where $\Delta H^{\dagger}$ and $\Delta S^{\dagger}$ are the enthalpy and entropy of activation, respectively. Eq. (11) is called Eyring equation and its logarithmic form can be written as:

$$\ln\left(\frac{k}{T}\right) = -\frac{\Delta H^{\dagger}}{R}\cdot\frac{1}{T} + \frac{\Delta S^{\dagger}}{R} + \ln\left(\frac{k_B}{h}\right) \quad (12)$$

By considering k_{ap}, Eq. (12) can be rewritten as follows:

$$\ln\left(\frac{k_{ap}}{T}\right) = -\frac{\Delta H^{\dagger}}{R}\cdot\frac{1}{T} + \frac{\Delta S^{\dagger}}{R} + \ln\left(\frac{k_B}{h}\right) \quad (13)$$

The values of $\Delta H^{\dagger}$ and $\Delta S^{\dagger}$ for the sonocatalytic degradation of AR1 by ZnS-TNTs were calculated from the slope and intercept of the $\ln(k_{ap}/T)$-$1/T$ plot (Fig. S7), which respectively gave 10.12 kJ mol^{-1} and -233.96 J K^{-1} mol^{-1} values. This means that, the sonocatalysis process is endothermic ($\Delta H^{\dagger} > 0$) with increasing regularity at the interface of AR1 molecules/ZnS-TNTs catalyst ($\Delta S^{\dagger} < 0$). In addition, the calculation of $\Delta G^{\dagger}$ at different temperatures using the relationship of $\Delta G^{\dagger} = \Delta H^{\dagger} - T\Delta S^{\dagger}$ (78.84, 82.18 and 84.52 kJ mol^{-1} at 298, 308 and 318 K, respectively) disclosed that the involved process was not spontaneous.

3.6. Mechanism of the sonocatalytic process

As outlined in the introduction, the mechanism of the sonocatalytic processes is generally based on the hot-spot theory and the sonoluminescence phenomenon. According to various research papers (Adewuyi, 2001; Leong et al., 2011; Qiu et al., 2018; Franc and Michel, 2006; Prasannalakshmi and Shanmugam, 2017; Zhang et al., 2018a, 2018b; Zhao et al., 2019), simultaneous application of the ZnS-TNTs catalyst and US waves leads to degradation of AR1 through the following sequence of events:

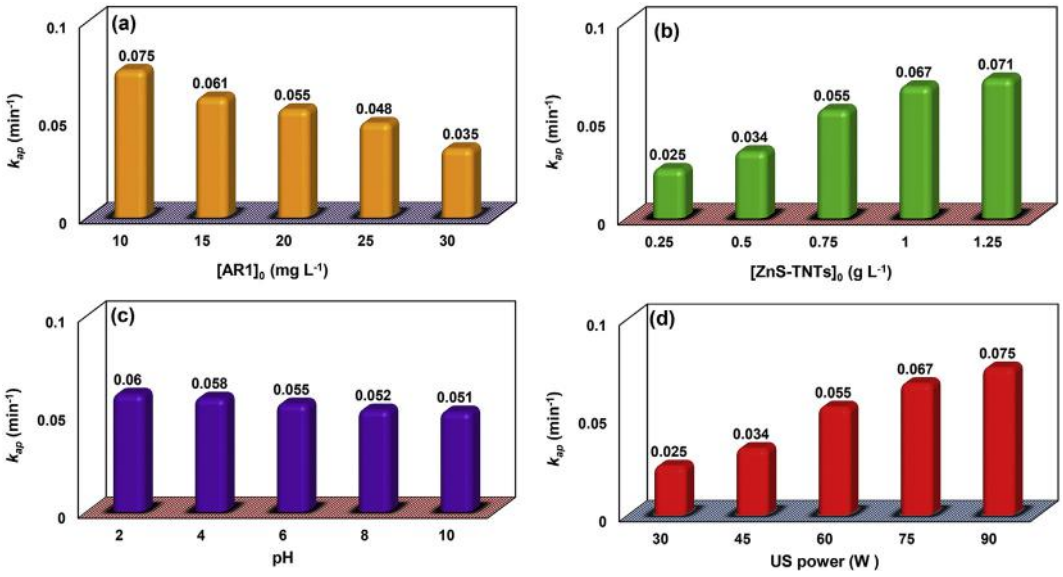

Fig. 9. The effect of operational parameters on k_{ap}.

1) Nucleation: ZnS-TNTs provide specific sites on its surface or liquid-solid phase boundaries for nucleation of bubbles. As a result, it contributes to formation, growth and collapse of bubbles in the cavitation process.
2) Sonoluminescence (SL): The SL phenomenon producing flashlights due to collapse of bubbles can lead to electromagnetic radiation in the range of 200–700 nm. As a result, ZnS and TNTs semiconductors are stimulated simultaneously, and e^--h^+ pairs are generated during a photocatalytic process.
3) Heat: The high local temperature resulting from cavitation phenomenon can lead to pyrolysis of water molecules and formation of °H and °OH, as well as thermal excitation of electron from the VB to the CB of the semiconductor catalyst during a thermocatalytic process.
4) Adsorption: The presence of TNTs with a high surface area in the composite structure increases the adsorption of dye molecules by ZnS-TNTs.

Regarding the described mechanism, the dye molecules are removed from the solution through adsorption onto the catalyst surface and degrade by the free radicals generated from the water pyrolysis and photo-thermal catalysis paths.

A major challenge in the aforementioned mechanism is to inhibit recombination of the photo-thermal generated e^--h^+ pairs. Electron-hole transfer in the heterojunction structure of ZnS-TNTs is undoubtedly a key step to achieve this goal. Since ZnS-TNTs composite is a Type-II heterojunction semiconductor (Prasannalakshmi and Shanmugam, 2017), the electrons in ZnS can transfer to TNTs and the holes follow a reverse migration, resulting in complete separation of holes and electrons.

To obtain more detailed sonocatalytic mechanism, influence of radical scavengers (benzoquinone and tert-butanol as a scavenger of $°O_2^-$ and °OH, respectively) was studied under RSM-based optimized conditions. It was turned out that the adding benzoquinone to the reaction medium causes a slight reduction in the sonocatalytic efficiency, while addition of tert-butanol impressively undermines the process (data not shown here). Inspired by these observations, the produced hydroxyl radicals play a crucial role in the sonocatalytic degradation of AR1 using ZnS-TNTs.

Scheme 1 illustrates the plausible mechanism, and Table S1 presents the reactions involved in this mechanism.

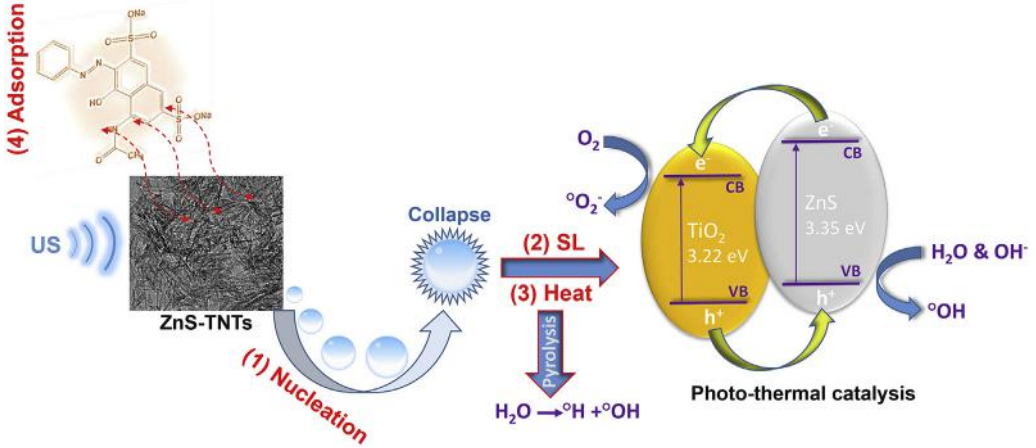

Scheme 1. Proposed mechanism for sonocatalytic degradation of AR1 by ZnS-TNTs.

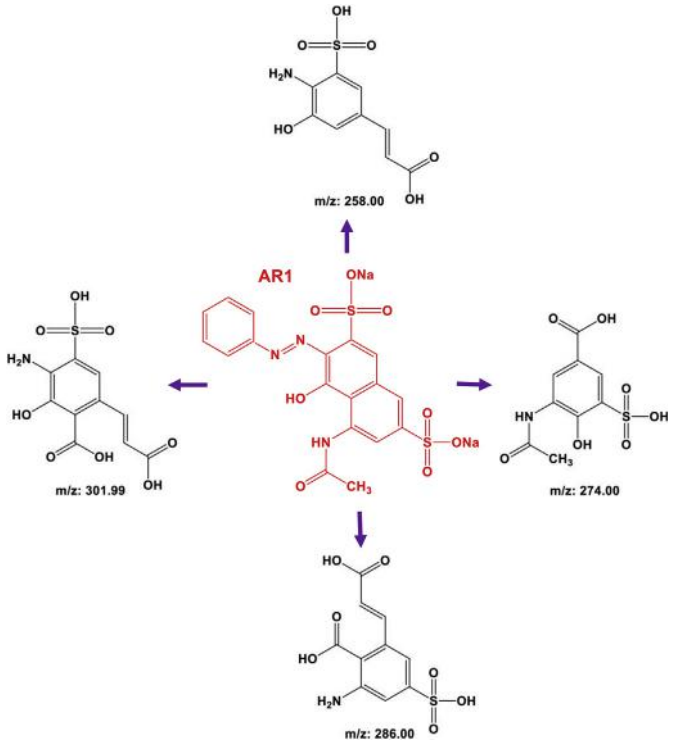

Fig. 10. Detected products during the sonocatalytic degradation of AR1.

3.7. Identification of by-products

The main products produced during the sonocatalytic degradation of AR1 by ZnS-TNTs were detected by the GC-MS analysis (Fig. 10). The resultant chromatogram along with the mass spectra concerning each peak are given in Figs. S8 and S9, respectively.

Evidently, the breakage of complex structure of AR1 was happened under the sonocatalytic process. A close observation of Fig. 10 revealed that, sonocatalytic degradation of AR1 was concurrently occurred with destruction of the benzene ring and cleavage of the −N=N- group.

4. Conclusion

According to the present research findings, it is concluded that the synthesized ZnS-TNTs has substantial potential for the sonocatalytic degradation of AR1 as an azo dye. CCD based on RSM was implemented for experimental design, and the results indicated that the degradation efficiency of AR1 increased with the increase of ZnS-TNTs amount, US power and time and reduced with the increment of its initial concentration. Under optimal conditions, the maximum degradation of 75.5% was obtained that was verified experimentally (73%). The optimized process was also studied from kinetics and thermodynamics perspectives. It was found that the kinetics data were consistent with the Langmuir–Hinshelwood pseudo-first-order model ($k_{ap} = 0.063$ min^{-1}). The results of the thermodynamics studies demonstrated that the involved process was endothermic and nonspontaneous. Furthermore, the mechanism of the sonocatalytic process was suggested with regard to sequence of events: nucleation, sonoluminescence, heat and adsorption. Finally, using the GC-MS technique, the main products of AR1 degradation were identified.

Acknowledgments

The authors would like to thank Tabriz Branch, Islamic Azad University for the financial support of this research, which is based on a research project contract.

Appendix A. Supplementary data

Supplementary data to this article can be found online at https://doi.org/10.1016/j.jclepro.2019.01.172.

References

Adewuyi, Y.G., 2001. Sonochemistry: environmental science and engineering applications. Ind. Eng. Chem. Res. 40, 4681–4715. https://doi.org/10.1021/ie010096l.

Aghaeinejad-Meybodi, A., Ebadi, A., Shafiei, S., Khataee, A.R., Rostampour, M., 2015. Modeling and optimization of antidepressant drug fluoxetine removal in aqueous media by ozone/H_2O_2 process: comparison of central composite design and artificial neural network approaches. J. Taiwan Inst. Chem. Eng. 48, 40–48. https://doi.org/10.1016/j.jtice.2014.10.022.

Aljerf, L., 2018. High-efficiency extraction of bromocresol purple dye and heavy metals as chromium from industrial effluent by adsorption onto a modified surface of zeolite: kinetics and equilibrium study. J. Environ. Manag. 225, 120–132. https://doi.org/10.1016/j.jenvman.2018.07.048.

Alwash, A.H., Jamalluddin, N.A., Ismail, N., Abdullah, A.Z., 2013. Sonocatalytic degradation of Acid Red dye in water using Fe-doped TiO_2 deposited on HY catalyst. In: Dev. Sustain. Chem. Bioprocess Technol. Springer, pp. 97–102. https://doi.org/10.1007/978-1-4614-6208-8_13.

Atkins, P., De Paula, J., 2009. Phys. Chem. 1. Thermodynamics and Kinetics.

Bezerra, M.A., Santelli, R.E., Oliveira, E.P., Villar, L.S., Escaleira, L.A., 2008. Response surface methodology (RSM) as a tool for optimization in analytical chemistry. Talanta 76, 965–977. https://doi.org/10.1016/j.talanta.2008.05.019.

Darvishi Cheshmeh Soltani, R., Safari, M., Mashayekhi, M., 2016. Sonocatalyzed decolorization of synthetic textile wastewater using sonochemically synthesized MgO nanostructures. Ultrason. Sonochem. 30, 123–131. https://doi.org/10.1016/j.ultsonch.2015.11.018.

Di Nica, V., Villa, S., Finizio, A., 2017. Toxicity of individual pharmaceuticals and their mixtures to Aliivibrio fischeri: experimental results for single compounds and considerations of their mechanisms of action and potential acute effects on aquatic organisms. Environ. Toxicol. Chem. 36, 807–814. https://doi.org/10.1002/etc.3568.

Eren, Z., Ince, N.H., 2010. Sonolytic and sonocatalytic degradation of azo dyes by low and high frequency ultrasound. J. Hazard Mater. 177, 1019–1024. https://doi.org/10.1016/j.jhazmat.2010.01.021.

Eskandarloo, H., Hashempour, M., Vicenzo, A., Franz, S., Badiei, A., Behnajady, M.A., Bestetti, M., 2016. High-temperature stable anatase-type TiO_2 nanotube arrays: a study of the structure–activity relationship. Appl. Catal. B Environ. 185, 119–132. https://doi.org/10.1016/j.apcatb.2015.11.048.

Fang, X., Zhai, T., Gautam, U.K., Li, L., Wu, L., Bando, Y., Golberg, D., 2011. ZnS nanostructures: from synthesis to applications. Prog. Mater. Sci. 56, 175–287. https://doi.org/10.1016/j.pmatsci.2010.10.001.

Franc, J.P., Michel, J.M., 2006. Fundamentals of Cavitation. Springer science & Business media, p. 76.

Grčić, I., Vujević, D., Žižek, K., Koprivanac, N., 2013. Treatment of organic pollutants in water using TiO_2 powders: photocatalysis versus sonocatalysis. React. Kinet. Mech. Catal. 109, 335–354. https://doi.org/10.1007/s11144-013-0562-5.

Khataee, A., Karimi, A., Woo Joo, S., 2016. Sonocatalytic degradation of Acid Red 17 in the presence of nanosized bio-silica: mechanism and kinetics. Curr. Nanosci. 12, 621–629. https://doi.org/10.2174/1573413712666160216233649.

Khataee, A., Saadi, S., Vahid, B., 2017. Kinetic modeling of sonocatalytic degradation of reactive orange 29 in the presence of lanthanide-doped ZnO nanoparticles. Ultrason. Sonochem. 34, 98–106. https://doi.org/10.1016/j.ultsonch.2016.05.026.

Laidler, K.J., King, M.C., 1983. Development of transition-state theory. J. Phys. Chem. 87, 2657–2664.

Ledakowicz, S., Żyła, R., Paździor, K., Wrębiak, J., Sójka-Ledakowicz, J., 2017. Integration of ozonation and biological treatment of industrial wastewater from dyehouse. Ozone Sci. Eng. 39, 357–365. https://doi.org/10.1080/01919512.2017.1321980.

Leong, T., Ashokkumar, M., Kentish, S., 2011. The fundamentals of power ultrasound-A review. Acoust Aust. 36, 54–63.

Miner, K.R., Blais, J., Bogdal, C., Villa, S., Schwikowski, M., Pavlova, P., Steinlin, C., Gerbi, C., Kreutz, K.J., 2017. Legacy organochlorine pollutants in glacial watersheds: a review. Environ. Sci. Process. Impacts. 19, 1474–1483. https://doi.org/10.1039/c7em00393e.

Pang, Y.L., Abdullah, A.Z., 2012. Comparative study on the process behavior and reaction kinetics in sonocatalytic degradation of organic dyes by powder and nanotubes TiO_2. Ultrason. Sonochem. 19, 642–651. https://doi.org/10.1016/j.ultsonch.2011.09.007.

Pang, Y.L., Abdullah, A.Z., 2013. Fe^{3+} doped TiO_2 nanotubes for combined adsorption-sonocatalytic degradation of real textile wastewater. Appl. Catal. B Environ. 129, 473–481. https://doi.org/10.1016/j.apcatb.2012.09.051.

Pang, Y.L., Abdullah, A.Z., 2013. Effect of carbon and nitrogen co-doping on characteristics and sonocatalytic activity of TiO_2 nanotubes catalyst for degradation

of Rhodamine B in water. Chem. Eng. J. 214, 129–138. https://doi.org/10.1016/j.cej.2012.10.036.
Pang, Y.L., Abdullah, A.Z., Bhatia, S., 2010. Comparison of sonocatalytic activities on the degradation of Rhodamine B in the presence of TiO_2 powder and nanotubes. J. Appl. Sci. 10, 1068–1075. https://doi.org/10.3923/jas.2010.1068.1075.
Pang, Y.L., Bhatia, S., Abdullah, A.Z., 2011. Process behavior of TiO_2 nanotube-enhanced sonocatalytic degradation of Rhodamine B in aqueous solution. Separ. Purif. Technol. 77, 331–338. https://doi.org/10.1016/j.seppur.2010.12.023.
Pang, Y.L., Lim, S., Ong, H.C., Chong, W.T., 2016. Synthesis, characteristics and sonocatalytic activities of calcined γ-Fe_2O_3 and TiO_2 nanotubes/γ-Fe_2O_3 magnetic catalysts in the degradation of Orange G, Ultrason. Sonochem 29, 317–327. https://doi.org/10.1016/j.ultsonch.2015.10.003.
Prasannalakshmi, P., Shanmugam, N., 2017. Fabrication of TiO_2/ZnS nanocomposites for solar energy mediated photocatalytic application. Spectrochim. Acta Part A Mol. Biomol. Spectrosc. 175, 1–10. https://doi.org/10.1016/j.saa.2016.12.018.
Qiu, P., Park, B., Choi, J., Thokchom, B., Pandit, A.B., Khim, J., 2018. A review on heterogeneous sonocatalyst for treatment of organic pollutants in aqueous phase based on catalytic mechanism. Ultrason. Sonochem. 45, 29–49. https://doi.org/10.1016/j.ultsonch.2018.03.003.
Ran, R., Meng, X., Zhang, Z., 2016. Facile preparation of novel graphene oxide-modified Ag_2O/Ag_3VO_4/$AgVO_3$ composites with high photocatalytic activities under visible light irradiation. Appl. Catal. B Environ. 196, 1–15. https://doi.org/10.1016/j.apcatb.2016.05.012.
Richards, W.T., Loomis, A.L., 1927. The chemical effects of high frequency sound waves. J. Am. Chem. Soc. 49, 3086–3089. https://doi.org/10.1021/ja01411a015.
Saratale, R.G., Saratale, G.D., Chang, J.S., Govindwar, S.P., 2011. Bacterial decolorization and degradation of azo dyes: a review. J. Taiwan Inst. Chem. Eng. 42, 138–157. https://doi.org/10.1016/j.jtice.2010.06.006.
Sen, S.K., Raut, S., Bandyopadhyay, P., Raut, S., 2016. Fungal decolouration and degradation of azo dyes: a review. Fungal Biol. Rev. 30, 112–133. https://doi.org/10.1016/j.fbr.2016.06.003.
Silva, L.G.M., Moreira, F.C., Souza, A.A.U., Souza, S.M., Boaventura, R.A.R., Vilar, V.J.P., 2018. Chemical and electrochemical advanced oxidation processes as a polishing step for textile wastewater treatment: a study regarding the discharge into the environment and the reuse in the textile industry. J. Clean. Prod. 198, 430–442. https://doi.org/10.1016/j.jclepro.2018.07.001.
Song, L., Zhang, S., Wu, X., Wei, Q., 2012. Synthesis of porous and trigonal TiO_2 nanoflake, its high activity for sonocatalytic degradation of rhodamine B and kinetic analysis. Ultrason. Sonochem. 19, 1169–1173. https://doi.org/10.1016/j.ultsonch.2012.03.011.
Thommes, M., Kaneko, K., V Neimark, A., Olivier, J.P., Rodriguez-Reinoso, F., Rouquerol, J., Sing, K.S.W., 2015. Physisorption of gases, with special reference to the evaluation of surface area and pore size distribution (IUPAC Technical Report). Pure Appl. Chem. 87, 1051–1069. https://doi.org/10.1515/pac-2014-1117.
Wang, J., Guo, B., Zhang, X., Zhang, Z., Han, J., Wu, J., 2005. Sonocatalytic degradation of methyl orange in the presence of TiO_2 catalysts and catalytic activity comparison of rutile and anatase. Ultrason. Sonochem. 12, 331–337. https://doi.org/10.1016/j.ultsonch.2004.05.002.
Wang, J., Jiang, Y., Zhang, Z., Zhang, X., Ma, T., Zhang, G., Zhao, G., Zhang, P., Li, Y., 2007. Investigation on the sonocatalytic degradation of acid red B in the presence of nanometer TiO_2 catalysts and comparison of catalytic activities of anatase and rutile TiO_2 powders. Ultrason. Sonochem. 14, 545–551. https://doi.org/10.1016/j.ultsonch.2006.09.004.
Wang, J., Lv, Y., Zhang, L., Jiang, R., Han, G., Liu, B., Wang, D., Zhang, X., 2010. Investigation on inorganic oxidant assisted sonocatalytic degradation of acid red B in the presence of nano-sized TiO_2 powder. Environ. Prog. Sustain. Energy 29, 443–449. https://doi.org/10.1002/ep.10428.
Yetim, T., Tekin, T., 2017. A kinetic study on photocatalytic and sonophotocatalytic degradation of textile dyes. Period. Polytech. Chem. 61, 102–108. https://doi.org/10.3311/PPch.8535.
Zhang, B., Li, J., Guo, L., Chen, Z., Li, C., 2018. Photothermally promoted cleavage of β-1, 4-glycosidic bonds of cellulosic biomass on Ir/HY catalyst under mild conditions. Appl. Catal. B Environ. 237, 660–664. https://doi.org/10.1016/j.apcatb.2018.06.041.
Zhang, R., Xu, J., Lu, C., Xu, Z., 2018. Photothermal application of $SmCoO_3$/SBA-15 catalysts synthesized by impregnation method. Mater. Lett. 228, 198–2002. https://doi.org/10.1016/j.matlet.2018.05.129.
Zhao, T., Xing, Z., Xiu, Z., Li, Z., Chen, P., Zhu, Q., Zhou, W., 2019. Synergistic effect of surface plasmon resonance, Ti^{3+} and oxygen vacancy defects on Ag/MoS_2/TiO_{2-x} ternary heterojunctions with enhancing photothermal catalysis for low-temperature wastewater degradation. J. Hazard Mater. 364, 117–124. https://doi.org/10.1016/j.jhazmat.2018.09.097.